Article

Transition Modeling for Low Pressure Turbines Using Computational Fluid Dynamics Driven Machine Learning

Harshal D. Akolekar[1],* , Fabian Waschkowski[1], Yaomin Zhao[2], Roberto Pacciani[3], and Richard D. Sandberg[1],*

1. Dept. of Mechanical Engineering, University of Melbourne, Victoria 3010, Australia
2. Center for Applied Physics and Technology, HEDPS, College of Engineering, Peking University, Beijing 100871, China
3. Dept. of Industrial Engineering, University of Florence, Italy
* Correspondence: hakolekar@student.unimelb.edu.au (HA); richard.sandberg@unimelb.edu.au (RS)

Abstract: Existing Reynolds Averaged Navier-Stokes based transition models do not accurately predict separation induced transition for low pressure turbines. Therefore, in this study, a novel framework based on computational fluids dynamics driven machine learning coupled with multi-expression and multi-objective optimization is explored to develop models which can improve the transition prediction for the T106A low pressure turbine at an isentropic exit Reynolds number of $Re_{2is} = 100,000$. Model formulations are proposed for the transfer and laminar eddy viscosity terms of the laminar kinetic energy transition model using seven non-dimensional pi groups. The multi-objective optimization approach makes use of cost functions based on the suction-side wall-shear stress and the pressure coefficient. A family of solutions is thus developed, whose performance is assessed using Pareto analysis and in terms of physical characteristics of separated-flow transition. Two models are found which bring the wall-shear stress profile in the separated region at least two times closer to the reference high-fidelity data than the baseline transition model. As these models are able to accurately predict the flow coming off the blade trailing edge, they are also able to significantly enhance the wake-mixing prediction over the baseline model.

Keywords: Machine Learning; Multi-objective optimization; Low Pressure Turbine; Transition; Turbulence Modeling

1. Introduction

As air travel is predicted to see continued growth, the aviation industry is focused on further improving the efficiency of gas turbines. Any technological advances which incrementally increase gas turbine efficiency can save millions of dollars, reduce carbon emissions, and create a sustainable future. One place to bring about such a change is at the grass root level of engine component design by understanding and enhancing the ability to model the flow physics of these components in an increasingly holistic, yet cheaper manner.

Low pressure turbines (LPT) are one of the most important components which drive the efficiency of gas turbines. If the efficiency of the LPT increases by 1% the specific fuel consumption will decrease by 0.6%-0.8% [1], translating to considerable fuel savings and emissions reductions, considering the volume of operations. LPT design and analysis is challenging as there is a large variation in flow physics between the aircraft taking off and entering cruise conditions. The Reynolds number of LPTs ranges from 0.5×10^5 at cruise to 5×10^5 at takeoff [2]. This causes a change in the boundary layers from turbulent at takeoff to transitional at cruise, which is the major portion of the flight. At lower Reynolds numbers (cruise), boundary-layer transition and separation play an important role in determining engine performance. There are three modes of transition: natural, bypass and separated-flow [3]. In LPTs, bypass and separated-flow transition are the most common transition modes. Natural transition begins with weak instabilities in

the laminar boundary layer which lead to three-dimensional instabilities resulting in turbulent spots [4]. However, when free-stream turbulence intensities are greater than 1%, boundary layers typically proceed from laminar to fully turbulent states without the occurrence of linear instabilities, thus bypassing various stages of natural transition. This is called bypass transition. Transition may also occur in the free shear-layer flow that results when a laminar boundary layer separates. The flow could reattach and form a laminar-separation / turbulent-reattachment bubble or could remain detached resulting in an open separation. Separated-flow transition occurs in regions of adverse pressure gradients near the leading edge or after peak suction in LPTs. Separated-flow transition also plays an important role in periodic unsteady transition wherein unsteady incoming wakes from previous blade rows interact with the separation bubble on the LPT suction-side [5]. Separated boundary layers with longer separation bubbles produce greater loss and cause larger deviation in exit flow angles[6], and are to be thus avoided.

With the increase of computational power, high-fidelity simulations [1,7] have become feasible that are able to accurately predict the transition phenomena. However, they are still not viable as an iterative industrial design tool, due to the associated high cost. Thus industry remains quite heavily dependent on RANS (Reynolds Averaged Navier-Stokes) calculations as they are a cost-effective way of modeling turbulent flows for engineering solutions. A number of transition models are at the disposal of turbomachinery designers [8]. The $\gamma - Re_\theta$ model [9] uses two transport equations for the intermittency (γ) and transition momentum thickness Reynolds number (Re$_\theta$), in addition to the turbulent kinetic energy (TKE) and specific dissipation. A class of models use the laminar kinetic energy (LKE) concept [10,11], wherein an additional transport equation is solved for the LKE. The $k\bar{v}_2\omega$ model solves an additional transport equation for $\bar{v}_2$ which represents wall-normal velocity fluctuations responsible for transition initiation. However, all of these existing RANS-based transition models struggle to accurately predict the onset and extent of separation on the suction-side of the aft portion of the LPT blade. Therefore, novel methods and models have to be explored in order to enhance the accuracy of transition prediction in the context of RANS.

Data-driven turbulence modeling is a field that has gained tremendous momentum in recent years [12]. In fact, many leading researchers [13–15] view data-driven turbulence modeling as a promising avenue for bridging the gap between the accuracy of high and low fidelity simulations, while maintaining the same order of cost as low-fidelity calculations. With the help of machine learning processes, high-fidelity data sets can be harvested to extract meaningful physics-based insights to improve the accuracy of RANS calculations. A host of different data-driven approaches have been applied to a large variety of industrially relevant cases. Neural networks embedding Galilean invariance to modify the anisotropy tensor were proposed by Ling et al. [16]. With these neural networks they improved the Reynolds stress and velocity field predictions over linear eddy viscosity models for duct flows and flow over wavy walls. Milani et al. [17] extended the work of Ling et al. [16] and developed a deep neural network to model the scalar-flux of turbulent diffusivity for two different jets in crossflow. Milani et al. [18,19] also used random forests to improve heat-flux modeling for film cooling applications. A more comprehensive overview of existing data-driven methods for turbulence model development can be found in Refs. [12,20,21].

It is evident that neural networks are the most popular way to improve the Reynolds stress and mean flow prediction. However, one major drawback lies in their 'black box' nature – they are difficult to interpret as physics-based information remains hidden in the network. An alternative that addresses this issue is symbolic regression which produces interpretable and explicit model forms. Ferreria [22] introduced gene expression programming (GEP) which was a new evolutionary algorithm for solving regression based problems. Weatheritt and Sandberg [23] developed GEP for turbulence modeling, which creates Galilean invariant turbulence closures, also known as explicit algebraic Reynolds stress models (EARSM). The GEP algorithm for turbulence model development produces

tangible symbolic expressions which can be correlated to physical phenomena and can be directly inserted into RANS codes. For example, Akolekar et al. [24] correlated different models from GEP to physical mechanisms such as laminar separation and wake-wake interactions in LPTs with unsteady inflow conditions using a zonal model development approach.

GEP also offers the added advantage of less computational cost over neural networks, both in the development and implementation phases. GEP has been successfully applied to a number of canonical and industrial (complex flows) turbulence modeling problems by enhancing the flow prediction capability for RANS and LES. Akolekar et al. [25] developed EARSMs for enhancing the prediction of LPT wake flow originating from open and closed separated boundary layers using 'frozen'[1] [26] high-fidelity databases. They also tested these EARSMs successfully on high-pressure turbine (HPT) flows [27], thus demonstrating the robustness of the models developed. Weatheritt et al. [28] developed GEP-based EARSMs for HPTs and assessed their performance in an *a-priori* sense. Recently, Zhao et al. [29] introduced a novel 'CFD-driven' (computational fluid dynamics) framework for turbulence model development based on GEP. This algorithm uses RANS feedback as part of the model training process. It was found that this method has high potential for offering robust turbulence closures to enhance the wake mixing prediction across different high and low pressure turbine operating conditions and blade geometries [30]. Waschkowski et al. [31] recently proposed a multi-objective and multi-expression extension to the 'CFD-driven' framework. The multi-objective approach makes use of different cost functions simultaneously whereas the multi-expression capability develops coupled turbulence closures across different regions of the flow field.

Efforts to enhance the accuracy of transition modeling with machine learning have only recently begun. Zafar et al. [32] developed a convolutional neural network based transition model capable of accurately predicting the transition onset location for incompressible, two-dimensional attached flows in a physically informed manner, without requiring direct computations, from linear instability theory. Yang and Xiao [33] developed a framework to improve transition models using field inversion and machine learning for airfoils. There are no studies, however, to improve the transition prediction for LPTs using machine learning.

This study, therefore, proposes a novel machine learning framework to generate models which enhance the prediction of separated-flow transition in LPTs. First of all, a brief overview of the LKE transition model [11], which is the baseline model used in this study, is presented. The functional forms of the LKE model's production and transfer terms are then modified using non-dimensional pi groups [34] based on local flow quantities. An extensive discussion ensues on the scientific ideology of making use of these particular pi groups. Using the recently developed multi-objective cost function based GEP algorithm [31] and the 'CFD-driven' [29] framework, models which enhance the separated-flow transition are proposed. The performance of these models is evaluated in terms of Pareto analysis and physical characteristics such as wall-shear stress, blade loading and turbulent wake mixing.

2. Transition Modeling

The LKE transition model [11] is used as the baseline model. This section discusses the transport equations used for the LKE transition model. It also discusses the intricacies of making possible improvements in the LKE model using non-dimensional pi groups.

2.1. Laminar Kinetic Energy Model

This study makes use of a transition model developed by Pacciani et al. [11] which is based on the LKE concept, as introduced by Mayle and Schulz [35], and takes into

---

[1] The 'frozen' methodology only solves the RANS equations for those quantities which cannot be directly obtained from a high-fidelity database. For example, the specific dissipation rate (ω) is not readily available from a high-fidelity database and is thus derived from a RANS calculation while keeping all other values constant – i.e., as derived from high-fidelity calculations.

account the pre-transitional rise of the fluctuating kinetic energy. The modeled transport equation for the LKE (k_l), with ν as the kinematic viscosity, is

$$\frac{Dk_l}{Dt} = P_l - 2\nu\frac{k_l}{y^2} + \nu\nabla^2 k_l - R. \tag{1}$$

The gradual rise of pre-transitional energy in the separated region is modeled using a production term (P_l) based on the mean shear rate (S) and a laminar eddy viscosity concept [36]. It is expressed as

$$P_l = \nu_l S^2, \tag{2a}$$

$$\nu_l = C_1 f_1 \sqrt{k_l}\delta_\Omega, \tag{2b}$$

$$f_1(Tu) = max\left[0.8, 2.0 \cdot tanh\left(\left(\frac{Tu}{4.5}\right)\right)\right], \tag{2c}$$

$$\delta_\Omega = max_y\left(\frac{U}{\Omega}\right), \tag{2d}$$

where ν_l is the laminar eddy viscosity, $C_1 = 0.01$, f_1 is defined as a function of the inlet free-stream turbulence intensity (Tu), δ_Ω is the maximum in the normal-to-the-wall direction shear-layer vorticity thickness which is assumed as a length scale representative of separated laminar flow, and l is a proper length scale, characteristic of the transition mode to be represented (natural, bypass or separated-flow). Ω is the vorticity magnitude and U is the magnitude of velocity. The choice of a vorticity-based length scale for the LKE production term was motivated by the fact that the most unstable wavelength in the separated shear-layer is related to the shear-layer thickness. The fluctuating energy is then gradually transferred to the turbulence field via a transfer term (R) which is defined as

$$R = C_2\beta^* f_2\omega k_l, \tag{3a}$$

$$f_2 = 1 - e^{-\psi/C_3}, \tag{3b}$$

$$\psi = max(0, R_y - C_4), \tag{3c}$$

$$R_y = \frac{\sqrt{k}y}{\nu}, \tag{3d}$$

with $C_2 = 0.3$, $C_3 = 8$, $C_4 = 10$, $\beta^* = 0.09$, f_2 is a damping function and R_y is the wall distance Reynolds number with y as the wall-normal wall distance. The quantity ψ can be considered as the transition parameter as it controls the transfer of energy from the laminar to the turbulent state, which occurs when the wall distance Reynolds number R_y reaches the threshold value of C_4. The term R appears in both laminar and TKE (k) transport equations which indicates no net change in the total fluctuating kinetic energy. This term implies that there is a transfer of energy from k_l to k. The TKE transport equation is written as

$$\frac{Dk}{Dt} = P_k - \beta^* f_k k\omega + \frac{\partial}{\partial x_j}\left[(\nu + \sigma_k \nu_T)\frac{\partial k}{\partial x_j}\right] + R, \tag{4}$$

where $\sigma_k = 0.5$ and the TKE production (P_k) is modeled as

$$P_k = \tau_{ij}\frac{\partial u_i}{\partial x_j} = f_\mu \nu_t S^2, \tag{5}$$

where τ_{ij} is the Reynolds stress tensor from the Boussinesq approximation [37], S is the magnitude of the strain-rate tensor and ν_T is the turbulence eddy viscosity. The closure damping functions are

$$f_\mu = 1 - 0.975 \, exp\left(\frac{-Re_T}{2.5}\right); \quad f_k = 1 - 0.722 \, exp\left[-\left(\frac{Re_T}{4.5}\right)^4\right], \tag{6}$$

where Re_T is the turbulence Reynolds number and is equal to $k/(\nu\omega)$. The transport equation of the specific dissipation rate is given as

$$\frac{D\omega}{Dt} = \alpha\frac{\omega}{k}P_k - \beta\omega^2 + \frac{\partial}{\partial x_j}\left[(\nu + \sigma_\omega \nu_T)\frac{\partial\omega}{\partial x_j}\right], \tag{7}$$

with $\alpha = 3/40$, $\beta = 5/9$ and $\sigma_\omega = 0.5$.

2.2. Proposed Model Formulation

In the LKE transition model, the LKE production (P_l) and transfer (R) terms play a crucial role in determining the transition onset and extent. It is proposed in this study to modify certain parts of these terms. The scientific ideology as well as the method of achieving this is discussed below.

2.2.1. Scientific Ideology

The LKE model, with some success, has been applied to the prediction of separated-flow transition in LPT cascades by Pacciani et al. [11,38], where the vorticity thickness of the separated shear-layer has been assumed as a length scale. However, the eddy viscosity equation (Eq. 2a) has two significant drawbacks. Firstly, it involves non-local quantities (e.g. the shear-layer vorticity thickness). Secondly, it does not account for the free-stream turbulence level. This latter deficiency was addressed by introducing the function f_1, which is expressed in terms of the inlet free-stream turbulence intensity Tu. Such a modification yielded satisfactory results on isolated cascades, as shown in Pacciani et al. [39]. However, the ν_l term has to consequently be modified in order to include only local quantities.

The transfer term R is formulated as in Walters and Cokljat [10]. Equation 3a has proven to be reliable in RANS calculations of separated-flow transition as it results in separation bubble lengths, transition onset locations, and pressure recovery prior to reattachment that are in good agreement with experimental data [11,38]. On many accounts, it is observed that the transition onset is dependent on the Reynolds number, pressure gradient and free-stream turbulence intensity. It is therefore argued that the term $R_y - C_4$ in the ψ function is too crude for triggering the transition onset. A better formulation, which is representative of the flow physics, has to be found for ψ.

In addition, the LKE model [11] was conceived for separated-flow transition prediction as the adopted length scale is a useful measure of the most unstable Kelvin-Helmholtz modes. The length scale also bears a loose relation with fluctuations developing in attached boundary-layers (Tollmien–Schlichting waves and Klebanoff streaks). A step forward towards a true LKE-based multi-mode model requires a more general framework that is able to address the growth of pre-transitional fluctuations in attached and separated boundary layers under the effects of the turbulent scales coming from the free-stream. Therefore, we propose the use of non-dimensional pi groups in order to modify certain terms of the LKE model. The use of machine learning (see section 3) will make the process more efficient and holistic.

2.2.2. Non-Dimensional Pi Groups

The transition problem is based on a number of local independent dimensional variables. In order to best capture the effect of these independent dimensional variables on the dependent variables (for example, the ψ term), the Buckingham pi theorem [34] is used to create dimensionless groups, called pi groups. Seven non-dimensional pi groups have been considered as possible input parameters to modify the LKE production term (Eq. 2) and the transfer term (Eq. 3) as

$$\Pi_1 = \frac{k_l}{\nu\Omega}; \quad \Pi_2 = \frac{\Omega y}{U}; \quad \Pi_3 = \frac{y}{l_t}; \quad \Pi_4 = \frac{\sqrt{k}y}{\nu}; \tag{8a}$$

$$\Pi_5 = \frac{k}{\nu\Omega}; \quad \Pi_6 = \frac{Sy}{U}; \quad \Pi_7 = \frac{\omega}{\Omega}, \tag{8b}$$

where ν is the kinematic viscosity and the turbulence length scale is defined as $l_t = \frac{\sqrt{k}}{\omega}$. The particular choice for the pi groups is motivated by their widespread use as transition sensor functions in a variety of models (Π_4, Π_5, and Π_6 [8]), by their nature of scale-determining terms for laminar fluctuations (Π_1, Π_2 and Π_6), or for turbulent fluctuations coming from the free-stream (Π_3 and Π_7).

Based on the shortcomings of the LKE model (section 2.2.1), we propose to modify the laminar eddy viscosity (ν_l) term from the LKE production term (P_l) and the transition parameter (ψ) from the transfer term *(R)* using the non-dimensional pi groups. If a local formulation for ν_l has to be found in terms of non-dimensional pi groups and local flow quantities, it can be represented as

$$\nu_l = f_{1a} y \sqrt{k_l}, \tag{9}$$

where $f_{1a} = f(\Pi_i)$. The machine learning processes in the model development process are tasked to find an expression for f_{1a} based on symbolic regression. There is no restriction on the order or the number of terms in the expression of f_{1a}. In order to ensure realizability of the production term, only the terms which ensures $f_1 > 0$ are selected for model evaluation; which is enforced by a limiter. It was also found that in order to keep an upper limit on the value of f_{1a}, an additional limiter $min(f_1, f_{1a})$ is also used. This limiter ensures stability and ease of convergence in the calculations. It also ensures that f_{1a} is activated only in the regions of interest, and not everywhere, as will be evident in section 5.2.3.

In its current form, ψ can be represented in terms of the non-dimensional pi groups as $\psi = max(\Pi_4 - C_4, 0)$. Initially, an attempt was made to find an expression for ψ without the use of a limiter. However, it was found that it was creating non-physical and unstable solutions in the laminar boundary layer as it was activating the transfer term which should be zero in the laminar boundary layer. Another consideration was to model the entire transfer term *(R)*, however, the machine learning algorithm was not proposing a transfer function which would tend to zero when moving closer towards the wall. A consideration was also made on whether either only the LKE production term or transfer term can be modified, without modifying the other one. However, since there is strong coupling between the two terms, both of them have to be modified together. Therefore, using any linear or non-linear combination of the non-dimensional pi groups, an expression is to be found for

$$\psi = max(f_{2a}(\Pi_i), 0). \tag{10}$$

3. Machine Learning Framework

This section discusses the various aspects of the machine learning transition modeling framework. The advantages of the 'CFD-driven' algorithm and the extensions by Waschkowski et al. [31] are explained. The methodology of this framework is also elucidated.

3.1. Advantages

GEP-based EARSM development had been centered around the 'frozen' approach [24,25] until the integration of CFD with GEP was made by Zhao et al. [29]. The 'CFD-driven' approach is feasible with GEP, because the GEP algorithm returns explicit model equations that can be instantly and automatically be implemented into RANS

solvers during the model development process. Since RANS calculations are then performed as part of the training loop, the resulting 'CFD-driven' models are tested in their target environment and are thus ready to be directly implemented into industrial design tools. Another advantage of the 'CFD-driven' training is that the definition of the cost function is more flexible as compared to the 'frozen' approach. Rather than being restricted to the quantities that can be directly calculated from the model equations, such as the anisotropy tensor or TKE production, the cost functions used in the 'CFD-driven' approach can be tailored to capture any important flow feature of interest. One can specify any mean or secondary statistic profiles in order to derive a suitable model. In fact, if large databases of high-fidelity data are unavailable and only few experimental or high-fidelity profiles are available, this approach has the potential to offer suitable models based on this limited data. This approach also ensures that the models generated are numerically stable as they have already been executed in CFD calculations. This 'CFD-driven' framework has so far been successfully applied to turbulence model improvement for wake mixing problems [29,30].

All current machine learning frameworks in the context of data-driven turbulence modeling, including GEP-based model development (both 'frozen' and 'CFD-driven'), are limited to developing one model per training run and only use one cost function (or a single training objective). However, the recent study of Waschkowski et al. [31] introduced multi-expression and multi-objective capabilities as extensions to the 'CFD-driven' approach to overcome these limitations. By developing expressions for multiple models, e.g. an anisotropy and a turbulence heat flux model, simultaneously and assigning a shared cost function value to the trained models, multi-expression training is capable to take the coupling effects of these models on the RANS predictions into account. This extension derived significantly improved turbulence models for a vertical natural convection flow with strongly coupling momentum and thermal fields. The second extension by Waschkowski et al. [31] has made the use of multiple cost functions feasible for the 'CFD-driven' framework. A multi-objective optimization algorithm based on the concept of Pareto dominance was implemented. Previously, with only one cost function available, several quantities of interest were combined into a composite function, which required weighting these quantities before training. The multi-objective extensions allows a trade-off between the cost functions after analysing the training results. Additionally, this extension yields a diverse set of candidate solutions, which was demonstrated to be an important asset in order to select physically plausible models.

3.2. Methodology

Figure 1 depicts the methodology of the transition modeling framework used in this study. Initially, a population of candidate models is created. In contrast to
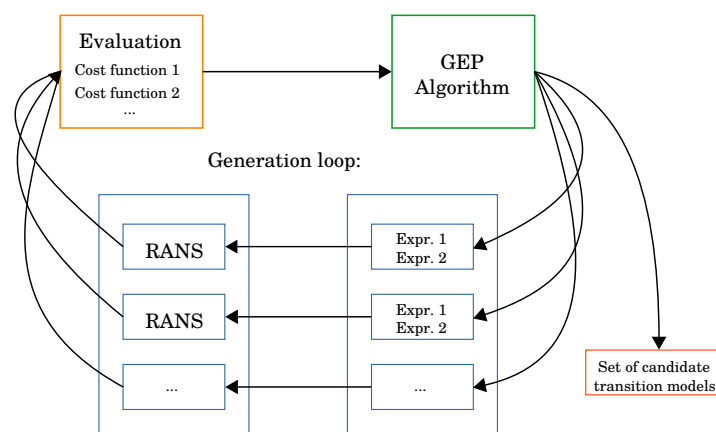

Figure 1. 'CFD-driven' transition model development with the multi-objective and multi-expression approach.

previously developing EARSMs, the GEP algorithm formulates two expressions per candidate solution – one each for f_{1a} and f_{2a}. The 'CFD-driven' approach reads the candidates' functional forms into RANS solvers and performs a series of RANS-based CFD calculations in parallel. The converged CFD solutions are then evaluated against one or more cost functions. This work makes use of two cost functions – the normalized mean squared errors between RANS and time-averaged high-fidelity data of the wall-shear stress and the pressure coefficient. Section 5.2.1 discusses these cost functions in greater detail. Finally, based on the cost function values or fitness of the candidate models, a new generation of candidates is formed through natural selection and genetic modifications (refer to [23,40] for additional details). The updated models are evaluated again through integrated CFD calculations. This training process iterates and the population of candidate models evolves over numerous generations.

4. Numerical Setup & Configuration

The numerical setup and the flow configuration are briefly discussed in this section. The T106A LPT linear cascade is used to develop transition models with the 'CFD-driven' multi-objective framework. Steady, compressible and 2D RANS calculations with steady inflow conditions were conducted using the TRAF solver [41]. The focus of this study was the midspan section of the T106A LPT blade which is the highest source of loss [6] in an LPT cascade. The midspan section can be approximated as 2D (quasi-3D) case.
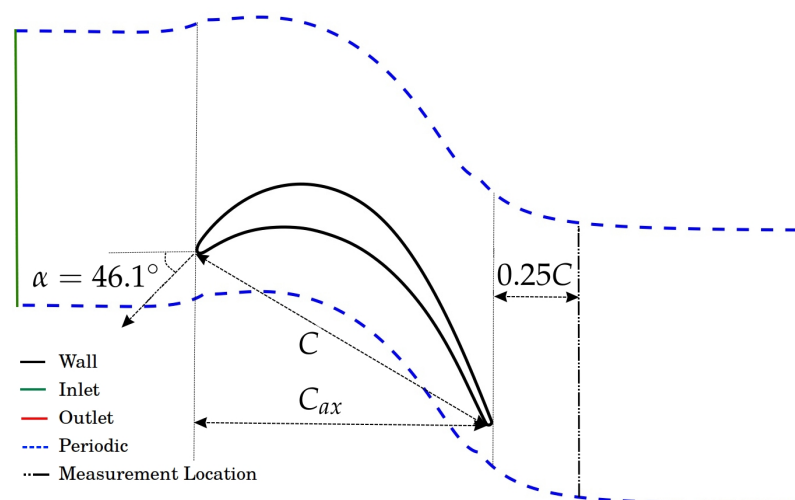

Figure 2. The T106A blade geometry and computational domain with boundary conditions.

The flow configuration was chosen so that the inflow conditions, Reynolds number and Mach number match the experimentally-validated direct numerical simulation (DNS) data of Michelassi et al. [1]. The isentropic exit Reynolds number and Mach numbers are $Re_{2is} = 100,000$ and $Ma_{2is} = 0.4$, respectively. The inlet free-stream turbulence intensity (Tu) is set to 4%.

Figure 2 shows the LPT domain used. At the inlet, the stagnation pressure and temperature along with the direction of the velocity vector (46.1° anti-clockwise from the horizontal at the blade leading edge) is specified. The upper and bottom edges of the domain have pitch-wise periodic boundary conditions. The grid, which has been used for previous studies [30,40], has approximately 83,000 points in the domain, with an O block around the blade and an H-block stitched on for the wake region. There are more than 30 points in the boundary layer with a $y^+ < 1$ for the first-off-the-wall points on both sides of the blade. An extensive grid convergence study for this grid was conducted in Ref. [40]. All the viscous terms for the RANS calculations are discretized using second order central difference schemes whereas the inviscid fluxes use a second order cell-centred scheme for discretization.

5. Results & Discussions

Using single and multi-objective optimization, models are developed using the machine-learning framework outlined in section 3 for the T106A LPT linear cascade at $Re_{2is} = 100,000$. This section discusses the performance of the models developed in terms of mean quantities such as the wall-shear stress, pressure coefficient and stagnation pressure loss profiles. Pareto analysis is also conducted to discuss the performance of the models developed via multi-objective optimization.

5.1. *Single-Objective Optimization*

Initially, a single-objective cost function was used to develop expressions for f_{1a} and f_{2a}. The baseline RANS case, cost function used, and the performance of the developed model are discussed in this section.

5.1.1. Baseline RANS Calculation

Figure 3 shows the suction-side wall-shear stress (τ_w) from the baseline RANS case (i.e. using the LKE model with the relations outlined in section 2.1) and DNS data [1]. At $Re_{2is} = 100,000$, the boundary layer separates and then reattaches, thus depicting a closed separation. From Figure 3 it is also very clear that the current baseline model does not predict the wall-shear stress accurately. What matters the most from the perspective of the boundary layer loss and subsequent downstream wake mixing loss is the accuracy of the prediction of the wall-shear stress close to and downstream of the separation onset ($x/C_{ax} \approx 0.84$).
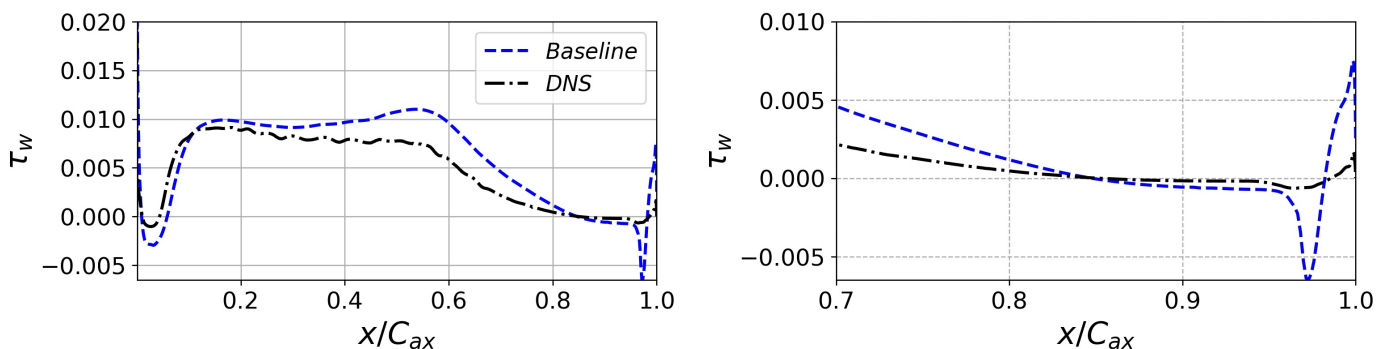

Figure 3. (a) Suction-side wall-shear stress from the baseline LKE model and DNS. (b) Zoomed view of the wall-shear stress in the separated flow region, near the blade trailing edge.

From Figure 3, the baseline LKE model offers a suitable prediction of the separation onset and extent, although the predicted reattachment occurs slightly earlier than for the high-fidelity data. The transition location, which occurs at the minimum wall-shear stress ($x/C_{ax} = 0.972$), is predicted quite closely with respect to the DNS data. However, there is still plenty of scope to improve the prediction of the wall-shear stress in the separated flow regions, especially in the region leading to and immediately after the transition location (i.e. overshooting in the wall-shear stress profile).

5.1.2. Cost Function

Initially, a single-objective cost function was used in the 'CFD-driven' framework. This cost function revolved around minimising the difference between the wall-shear stress obtained from RANS with respect to the one from DNS. Since the main objective of this study is to improve the separation prediction, the wall-shear stress data from $0.75 \leq x/C_{ax} \leq 1$ was selected. The cost function (J^{SO}) using a single-objective function (SO-Model) is

$$J^{SO} = \sum_{x/C_{ax}=0.75}^{1} \left(\tau_w^{DNS} - \tau_w^{RANS} \right)^2. \tag{11}$$

5.1.3. Analysis of the SO-Model

The 'CFD-driven' framework was able to provide suitable functional forms for f_{1a} and f_{2a} that significantly reduced the value of J^{SO}. For the baseline case the value of the cost function is 4.147×10^{-6} and for the SO-model the value of J^{SO} is 0.192×10^{-6}. In order to obtain this solution, 90 generations, similar to the 'CFD-driven' model development for LPT wake mixing [30] were required with a population of 125 candidates. The new formulations of f_{1a} and f_{2a} were applied across the entire blade, even though they were developed using reference data from $0.75 \leq x/C_{ax} \leq 1$. The wall-shear stress plot is shown in Figure 4a and the pressure coefficient plot (C_p) is shown in Figure 4b. The framework produces a model that results in a close match with the DNS wall-shear stress in the separated-flow region. It even gets the reattachment location predicted correctly. Since the region immediately upstream of $x/C_{ax} = 0.75$, was not included in the cost function there is not much change in the wall-shear stress behaviour there. The SO-model, however, also improves the prediction of the leading-edge separation, even though that region was not included as part of the training data.
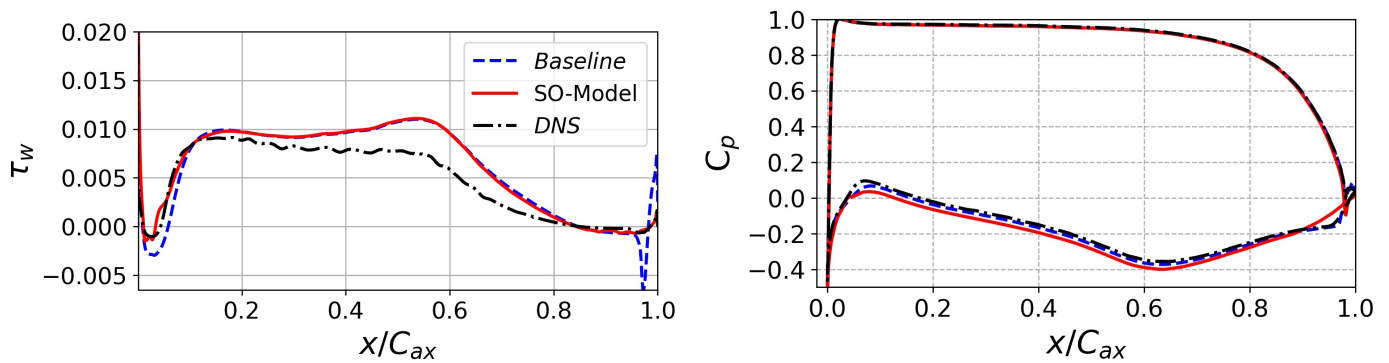

Figure 4. (a) Suction-side wall-shear stress and (b) pressure and suction-side pressure coefficient for the SO-Model, baseline case and DNS.

Even though the wall-shear stress prediction has improved with the SO-model, the pressure coefficient (C_p) distribution has worsened over the baseline case, especially in the separated flow region on the suction-side. As the baseline case and DNS both show, there should be a plateau in the pressure coefficient plot when the flow separates. The SO-model, unlike the baseline case, does not predict a strong peak in the separated flow region in the wall-shear stress plot. The strong peak in the wall-shear stress is a peculiarity of the LKE framework, as it is the result of the turbulence 'ignition' by the transfer term. In the authors' experience, the position of the minimum wall-shear stress and the subsequent ramp in wall-shear stress is crucial to get the correct pressure coefficient distribution in the separated region. As the SO-model does not show this behaviour, it tends to worsen the pressure coefficient predictions over the baseline case.

5.2. Multi-Objective Optimzation

Next, the multi-objective optimization approach is used to develop transition models. This section discusses the cost functions and the performance of the solutions obtained with respect to the cost functions and physical characteristics.

5.2.1. Cost Functions

The main motivation to explore the avenue of multiple cost functions was due to the worsening in the pressure coefficient prediction in the separation region on the suction-side over the baseline case when a single objective function was used. In order to at least maintain the pressure coefficient distribution as obtained from the baseline case, an additional cost function was created based on the pressure coefficient from close to

peak suction right to the blade trailing edge (TE)($0.6 \leq x/C_{ax} \leq 1$ – this region includes the separation plateau). The two cost functions used are

$$J^{MO1} = \sum_{x/C_{ax}=0.6}^{1} \left(\tau_w^{DNS} - \tau_w^{RANS} \right)^2, \tag{12a}$$

$$J^{MO2} = \sum_{x/C_{ax}=0.6}^{1} \left(C_p^{DNS} - C_p^{RANS} \right)^2. \tag{12b}$$

$$\tag{12c}$$

The multi-objective optimization was run for 90 generations with a population of 125 individuals. In order to obtain the final solution (at *n=90*), the multi-objective approach used about 1500 core hours which was about three times that of the single-objective approach. This is because the multi-objective approach evaluates many more possible candidate solutions as opposed to a single best solution in the single-objective approach. If the data from baseline RANS calculations are fed into the cost functions, then $J^{MO1} = 5.24 \times 10^{-6}$ and $J^{MO2} = 3.816 \times 10^{-4}$.

5.2.2. Pareto Analysis

The best way to analyse the evolution of the models generated with the multi-objective optimization approach is with Pareto analysis. In order to compare two candidate solutions, this optimization approach uses the concept of ==Pareto domination.== One candidate is said to dominate the other candidate when its cost function values are all lower or equal ($\leq$) to the dominated candidate's values with one value being strictly lower ($<$). When Pareto domination is applied to the entire population via pairwise comparison, each candidate solution is assigned a rank r. Within one rank, no solution dominates another solution. However, all solutions of rank $r = k_1$ dominate all solutions
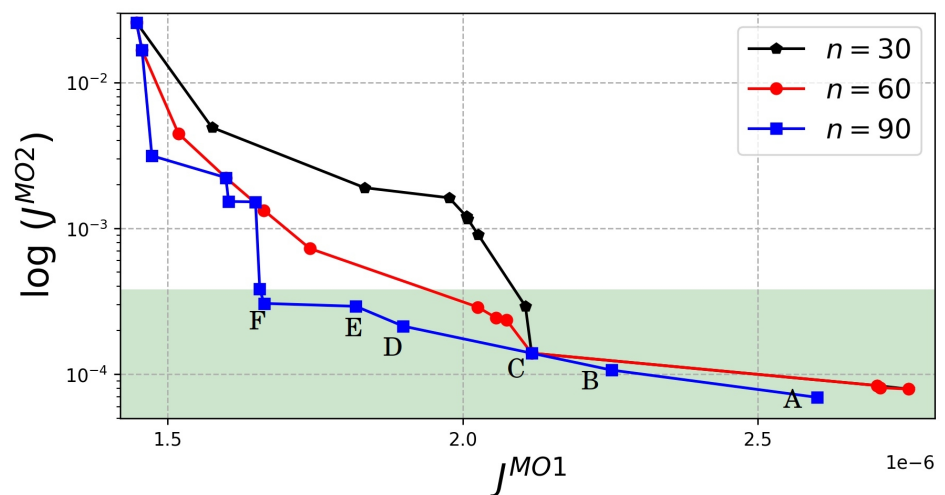

Figure 5. Pareto diagram showing the evolution of the Pareto front up to 90 generations.

of rank $r = k_2$, where k_1 and k_2 are integer values and $k_1 < k_2$. The solutions of rank $r = 1$ are not dominated by any other solution in the population and define what is commonly referred to as the Pareto front. Figure 5 shows the Pareto front evolution up to 90 generations (n). The value of J^{MO1} and the natural logarithm of J^{MO2} are shown on the x and y axes respectively. As the generations go on increasing, the number of candidate solutions on the Pareto front go on increasing, which indicates that a better set of solutions (in terms of the cost functions) are being found with each generation. The Pareto front shifts closer to the x and y axes indicating that the objective functions are being minimized with each progressive generation. At $n = 90$, all the solutions on

the Pareto fronts have a value of J^{MO1} which is more than two times smaller than the baseline case. However, not all solutions offer reductions in the value of J^{MO2} over the baseline case. The shaded green area in Figure 5 denotes the region in which the value of J^{MO2} is less than the baseline value of $J^{MO2} = 3.816 \times 10^{-4}$.

5.2.3. Analysis of Solutions

At the last generation (*n=90*), every model on the Pareto front was analysed for its performance in terms of the wall-shear stress and the pressure coefficient. It was found that only those models which reduced the value of J^{MO2} over the baseline case were able to produce numerically stable solutions. Of these, solutions *A* and *B* best represented the flow physics on the blade and in the wake. Although solutions *C-F* reduced the value of J^{MO2} over the baseline case and had lower values of J^{MO1} than solutions *A* and *B*, they either predicted an early transition onset location or they were unable to provide a strong peak in the separated region in the wall-shear stress profile (i.e. similar to the SO-model in Figure 4a). Absence of a strong peak in the separated flow region of the wall-shear stress profile, or predicting an early onset of transition as compared to the DNS data (even with a strong peak in the separated region) resulted in excessive turbulent diffusion and some numerical instabilities in the wake. The model formulation of solution *A* is

$$f_{1a} = \Pi_3(\Pi_2 + \Pi_4 - \Pi_3 - \Pi_7 + 2) + \Pi_2 - 0.21, \tag{13a}$$

$$\psi = max\left(1.16 - 0.43\Pi_1 + 0.21\Pi_5 - \Pi_6, 0\right). \tag{13b}$$

The formulation of the f_{1a} function highlights the leading role of the Π_2 term which is a vorticity scale closely related to the shear-layer vorticity thickness. This is consistent with the original modelling assumption. Π_2 and Π_4 introduce the effect of the freestream turbulence level in LKE production. The Π_7 term is large in the wall proximity and rapidly decays with the distance from the wall. It appears with a negative sign and so it tends to suppress LKE production near the wall. This is consistent with the fact that in separated laminar flows the amplification of pre-transitional fluctuations occurs in the separated shear-layer and thus far from the wall. The original formulation of the ψ function employs the wall distance turbulent Reynolds number (i.e. Π_4) to control the transition onset. In Equation 13b it is replaced by Π_5. Some recently developed transition prediction frameworks [8,10] share this particular feature with the proposed one. The transition onset parameter, which is originally a constant (i.e. C_4), is replaced in Equation 13b by a function of Π_1 and Π_6. The effect is to delay transition as the shear-layer thickness increases (e.g. long bubbles). Additionally, the limiter $min(f_1, f_{1a})$ was also used as part of the multi-objective calculations. The use of this limiter improved the stability of the solution in the wake region. Due to the use of this limiter, the leading-edge separation prediction did not change with respect to the baseline case.

Figures 6 and 7 show the pressure coefficient and suction-side wall-shear stress respectively for the baseline case, DNS data and the solutions *A* (MO-A) and *B* (MO-B). Both the solutions not only predict the separation plateau feature in the pressure coefficient plot, as opposed to the SO-model, but they also offer an improved prediction in the separation plateau over the baseline case. This is because both the MO-A and MO-B models predict a peak (of smaller magnitude than the baseline case) in the separated flow region of the wall-shear stress profile; a necessary characteristic of the LKE modeling framework to predict a separation plateau in the pressure coefficient. These models also offer significantly better predictions of the wall-shear stress over the baseline case. They reduce the magnitude of both peaks (one at transition onset and the other one after turbulent reattachment) in the wall-shear stress by more than two times over the baseline case. The MO-A and MO-B models predict reattachment at $x/C_{ax} = 0.987$ and $x/C_{ax} = 0.988$ respectively, which is quite close to the DNS value of $x/C_{ax} = 0.986$. This is an improvement over the baseline case which predicts reattachment at $x/C_{ax} = 0.982$. Consequently, these models have a positive impact on the wake mixing prediction.
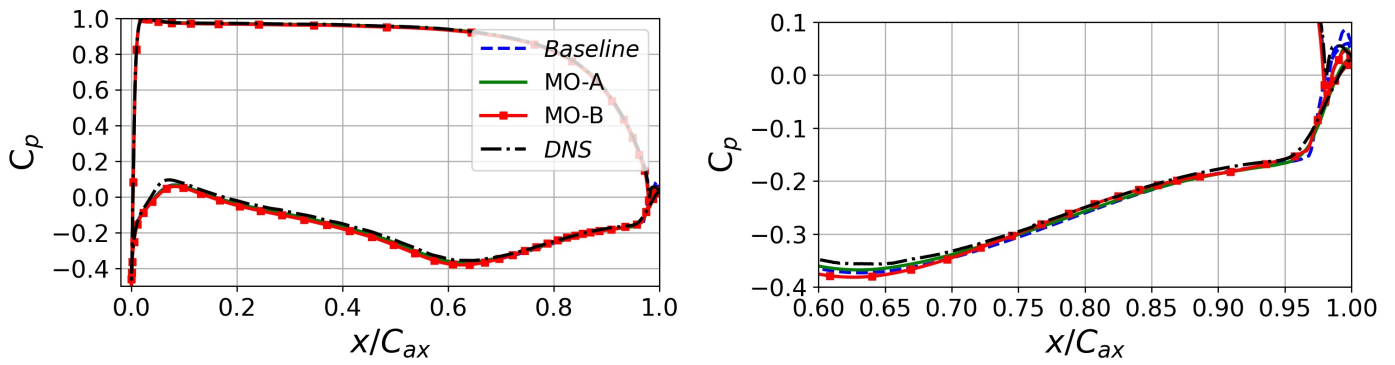
Figure 6. (a) Pressure coefficient with the various multi-objective optimized models. (b) Zoomed view of the suction-side pressure coefficient in the separated flow region, near the blade trailing edge.
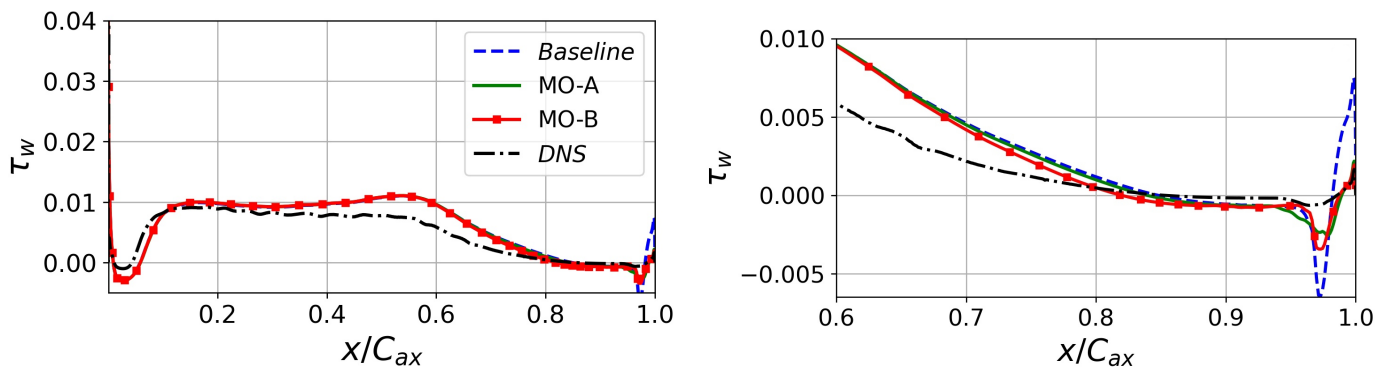
Figure 7. (a) Suction-side wall-shear stress with the various multi-objective optimized models. (b) Zoomed view of the suction-side wall-shear stress in the separated flow region, near the blade TE.

Figure 8 shows the stagnation pressure loss at 25%C downstream of the blade TE (see Figure 2). The stagnation pressure loss (Ω^*) is defined as

$$\Omega^*(y^*) = \frac{P_{t,1} - P_t(y^*)}{P_{t,1} - P_2}, \tag{14}$$

where $P_{t,1}$ is the inlet stagnation pressure, P_2 is the exit static pressure, $P_t(y^*)$ is the stagnation pressure at the location of interest and y^* is a pitchwise normalized coordinate defined as $y^* = (y - y_{max})/(y_{max} - y_{min})$. Since the MO-A and MO-B models are able to predict the flow coming off the blade TE quite accurately with respect to the high-fidelity data, the resulting stagnation pressure loss profiles (and thus the wake mixing) are also better predicted than the baseline case. These models improve the prediction of the peak wake loss error and also increase the width of the profile, indicating additional diffusion in the wake over the baseline case. It is to be noted that the Boussinesq approximation was used in the wake region for the baseline and MO models. The wake mixing prediction can be further improved by using machine-learnt EARSMs. However, further enhancing the wake mixing prediction was not addressed in this work, as this has been dealt with separately in Refs. [25,29,30]. The 'CFD-driven' canonical-wake EARSM of Akolekar et al. [30] is apt for further improving the wake mixing prediction for this particular case. The canonical-wake model has been formulated such that it can improve the wake evolution when the flow coming off the blade TE is accurately predicted.

In summary, including an additional cost function based on the suction-side pressure coefficient was an immense benefit to formulate models which not only preserve the integrity of the LKE modeling framework, but also improve the prediction of the
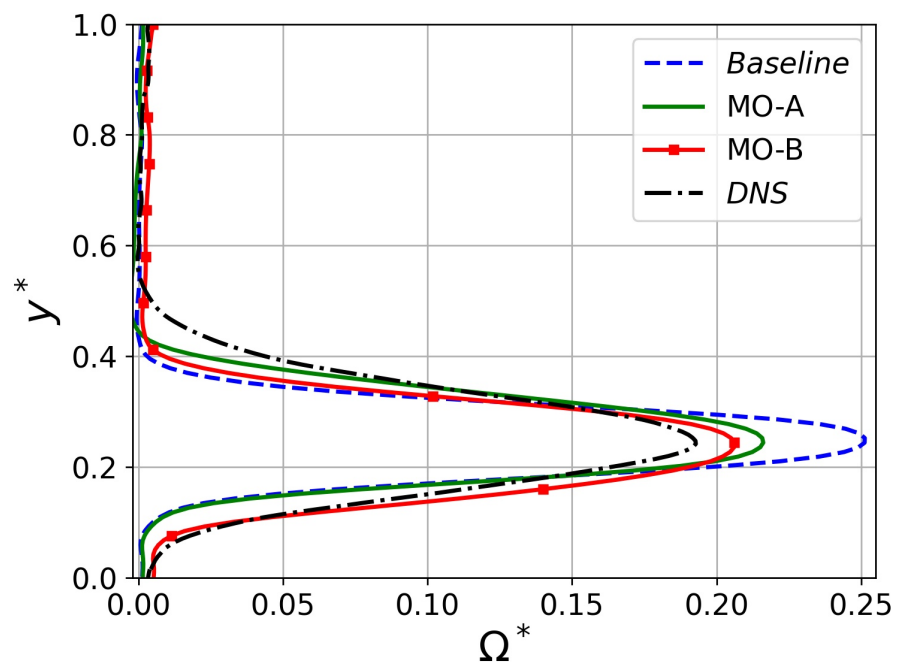
Figure 8. Stagnation pressure loss profiles 25%C downstream of the blade TE.

physical characteristics of the flow not only in the separation region but also downstream of the blade TE.

6. Conclusions

This study makes the use of a multi-objective 'CFD-driven' algorithm to enhance the prediction of separated flow transition of the T106A LPT blade at $Re_{2is} = 100,000$. The existing LKE transition model struggles to accurately predict the wall-shear stress in the separated flow region and thus the wake mixing downstream of the blade TE is also poorly predicted. Using the 'CFD-driven' multi-objective framework and seven non-dimensional pi groups, model formulations for the transition parameter ψ and the f_{1a} term in the laminar eddy viscosity are proposed. Initially, a single-objective approach was explored, using the wall-shear stress from DNS data in the separation region as a reference. The resulting SO-model was able to predict the wall-shear stress surprisingly close to the DNS. However, as there was no strong peak in the separation region of the wall-shear stress profile (which is a result of turbulence ignition by the transfer term), the prediction of the separation plateau in the pressure coefficient plot worsened over the baseline case.

In order to account for this deficiency of the SO-model, multi-objective optimization was used and an additional cost function which included the suction-side pressure coefficient was introduced. Pareto analysis was used to assess the performance of the models developed. It was found that only those models which reduced the value of the pressure coefficient cost function over the baseline case produced numerically stable solutions. Two of these models were able to preserve the integrity of the LKE framework (i.e. strong peak in the separated region) and also improved the prediction of physical characteristics of the transition process such as the reattachment location and magnitudes of the peaks in the wall-shear stress profile. Thus the overall structure of the separation bubble was improved. Since these models were able to closely match the flow coming off the blade TE, the resulting turbulent diffusion in the wake was increased. This resulted in better prediction of wake loss profiles with respect to high-fidelity data.

Overall, a promising framework of multi-objective 'CFD-driven' model development using non-dimensional pi groups has been explored. Additional analyses and development

is required to test this framework and resulting models across different operating conditions and geometries.

Abbreviations

The following abbreviations are used in this manuscript:

CFD	Computational fluid dynamics
DNS	Direct numerical simulation
EARSM	Explicit algebraic Reynolds stress model
GEP	Gene expression programming
LES	Large eddy simulation
LKE	Laminar kinetic energy
LPT	Low pressure turbine
MO	Multi-objective
RANS	Reynolds averaged Navier–Stokes
SO	Single-objective
TE	Trailing edge
TKE	Turbulent kinetic energy

References

1. Michelassi, V.; Chen, L.W.; Pichler, R.; Sandberg, R.D. Compressible Direct Numerical Simulation of Low Pressure Turbine - Part II: Effect of Inflow Disturbances. *Journal of Turbomachinery* **2015**, *137*, 71005.
2. Hodson, H.P.; Howell, R.J. Bladerow Interactions, Transition, and High-Lift Aerofoils in Low-Pressure Turbines. *Annual Review of Fluid Mechanics* **2005**, *37*, 71–98. doi:10.1146/annurev.fluid.37.061903.175511.
3. Mayle, R.E. The Role of Laminar-Turbulent Transition in Gas Turbine Engines. *Journal of Turbomachinery* **1991**, *113*, 509–537.
4. Schlichting, H.; Gersten, K. *Boundary Layer Theory*; Springer, 1999.
5. Stieger, R.D.; Hodson, H.P. The Transition Mechanism of Highly-Loaded LP Turbine Blades. *Journal of Turbomachinery* **2004**, *126*, 536–543.
6. Denton, J.D. The 1993 IGTI Scholar Lecture: Loss Mechanisms in Turbomachines. *Journal of Turbomachinery* **1993**, *115*, 621.
7. Michelassi, V.; Chen, L.; Pichler, R.; Sandberg, R.; Bhaskaran, R. High-Fidelity Simulations of Low-Pressure Turbines: Effect of Flow Coefficient and Reduced Frequency on Losses. *Journal of Turbomachinery* **2016**, *138*, 111006.
8. Dick, E.; Kubacki, S. Transition Models for Turbomachinery Boundary Layer Flows: A Review. *International Journal of Turbomachinery, Propulsion and Power* **2017**, *2*, 4.
9. Menter, F.R.; Langtry, R.B.; Likki, S.R.; Suzen, Y.B.; Huang, P.G. A Correlation-Based Transition Model Using Local Variables — Part I : Model Formulation. *J. Turbomach.* **2006**, *128*, 413–422.
10. Walters, D.K.; Cokljat, D. A Three-Equation Eddy-Viscosity Model for Reynolds-Averaged Navier-Stokes Simulations of Transitional Flow. *Journal of Fluids Engineering* **2008**, *130*, 121401.
11. Pacciani, R.; Marconcini, M. Calculation of High-Lift Cascades in Low Pressure Turbine Conditions Using a Three-Equation Model. *Journal of Turbomachinery* **2011**, *133*, 1–9. doi:10.1115/1.4001237.
12. Brunton, S.L.; Noack, B.R.; Koumoutsakos, P. Machine Learning for Fluid Mechanics. *Annual Review of Fluid Mechanics* **2020**, *52*, 477–508.
13. Duraisamy, K.; Spalart, P.R.; Rumsey, C.L. Status , Emerging Ideas and Future Directions of Turbulence Modeling Research in Aeronautics. Technical Report November, NASA, Hampton, USA, 2017.
14. Medic, G. Impact of Vision 2030 on CFD Practices in Propulsion Industry. we, 2019.
15. Runchal, A.K.; Rao, M.M. CFD of the Future: Year 2025 and Beyond. In *50 Years of CFD in Engineering Sciences*; Springer, 2020.

16. Ling, J.; Jones, R.; Templeton, J. Machine learning strategies for systems with invariance properties. *Journal of Computational Physics* **2016**, *318*, 22–35.

17. Milani, P.M.; Ling, J.; Eaton, J.K. Turbulent Scalar Flux in Inclined Jets in Crossflow: Counter Gradient Transport and Deep Learning Modelling. *Journal of Fluid Mechanics* **2021**, *906*, [2001.04600].

18. Milani, P.M.; Ling, J.; Saez-Mischlich, G.; Bodart, J.; Eaton, J.K. A Machine Learning Approach for Determining the Turbulent Diffusivity in Film Cooling Flows. *Journal of Turbomachinery* **2018**, *140*, 021006.

19. Milani, P.M.; Ling, J.; Eaton, J.K. Physical Interpretation of Machine Learning Models Applied to Film Cooling Flows. *Journal of Turbomachinery* **2019**, *141*, 011004.

20. Duraisamy, K.; Iaccarino, G.; Xiao, H. Turbulence Modeling in the Age of Data. *Annual Review of Fluid Mechanics* **2019**, *53*, 357–377.

21. Duraisamy, K. Machine Learning Augmented Reynolds-Averaged & Large eddy Simulation Models of Turbulence. *arXiv* **2021**, pp. 1–25, [arXiv:2009.10675v3].

22. Ferreira, C. Gene Expression Programming: a New Adaptive Algorithm for Solving Problems. *Complex Systems* **2001**, *13*, 87–129.

23. Weatheritt, J.; Sandberg, R.D. A Novel Evolutionary Algorithm Applied to Algebraic Modifications of the RANS Stress-Strain Relationship. *Journal of Computational Physics* **2016**, *325*, 22–37.

24. Akolekar, H.D.; Sandberg, R.D.; Hutchins, N.; Michelassi, V.; Laskowski, G. Machine-Learnt Turbulence Closures for Low Pressure Turbines with Unsteady Inflow Conditions. *Journal of Turbomachinery* **2019**, *141*, 101009.

25. Akolekar, H.D.; Weatheritt, J.; Hutchins, N.; Sandberg, R.D.; Laskowski, G.; Michelassi, V. Development and Use of Machine-Learnt Algebraic Reynolds Stress Models for Enhanced Prediction of Wake Mixing in Low-Pressure Turbines. *J. Turbomach.* **2019**, *141*.

26. Parneix, S.; Laurence, D.; Durbin, P.A. A Procedure for Using DNS Databases. *Journal of Fluids Engineering* **1998**, *120*, 40–46.

27. Akolekar, H.D.; Zhao, Y.; Sandberg, R.D.; Hutchins, N.; Michelassi, V. Turbulence Model Development for Low & High Pressure Turbines Using a Machine Learning Approach. 24th International Society of Air Breathing Engines; , 2019.

28. Weatheritt, J.; Pichler, R.; Sandberg, R.D.; Laskowski, G.; Michelassi, V. Machine Learning for Turbulence Model Development Using a High Fidelity HPT Cascade Simulation. ASME Turbo Expo 2017 Turbomach. Tech. Conf. Expo.; , 2017; pp. GT2017—63497.

29. Zhao, Y.; Akolekar, H.D.; Weatheritt, J.; Michelassi, V.; Sandberg, R.D. RANS Turbulence Model Development Using CFD-Driven Machine Learning. *Journal of Computational Physics* **2020**, *411*, 109413.

30. Akolekar, Harshal D..; Zhao, Y.; Sandberg, R.D.; Pacciani, R. Integration of Machine Learning and Computational Fluid Dynamics to Develop Turbulence Models for Improved Low Pressure Turbine Wake Mixing Predictions. *Journal of Turbomachinery* **2021**, *Accepted*.

31. Waschkowski, F.; Zhao, Y.; Sandberg, R.; Klewicki, J. Multi-Objective CFD-Driven Development of Coupled Turbulence Closure Models. *arXiv* **2021**, [2105.06225].

32. Zafar, M.I.; Xiao, H.; Choudhari, M.M.; Li, F.; Chang, C.L.; Paredes, P.; Venkatachari, B. Convolutional Neural Network for Transition Modeling Based on Linear Stability Theory. *Physical Review Fluids* **2020**, *5*, 1–15.

33. Yang, M.; Xiao, Z. Improving the k-ω-γ-Ar Transition Model by the Field Inversion and Machine Learning Framework. *Physics of Fluids* **2020**, *32*.

34. White, F.M. Fluid Mechanics **2017**.

35. Mayle, R.; Schulz, A. The Path to Predicting Bypass Transition. *Journal of Turbomachinery* **1997**, *119*, 405–411.

36. Lardeau, S.; Leschziner, M.A.; Li, N. Modelling Bypass Transition with Low-Reynolds-Number Nonlinear Eddy-Viscosity Closure. *Flow, Turbulence and Combustion* **2004**, pp. 49–76.

37. Schmitt, G. About Boussinesq's Turbulent Viscosity Hypothesis: Historical Remarks and a Direct Evaluation of its Validity. *Comptes Rendus Mecanique, Elsevier Masson* **2007**, *335*, 617–627.

38. Pacciani, R.; Marconcini, M.; Arnone, A.; Bertini, F. An Assessment of the Laminar Kinetic Energy Concept for the Prediction of High-Lift, Low-Reynolds Number Cascade Flows. *Proceedings of the Institution of Mechanical Engineers, Part A: Journal of Power and Energy* **2011**, *225*, 995–1003.

39. Pacciani, R.; Marconcini, M.; Arnone, A.; Bertini, F. Predicting High-Lift Low-Pressure Turbine Cascades Flow Using Transition-Sensitive Turbulence Closures. *Journal of Turbomachinery* **2014**, *136*.

40. Akolekar, H.D. Turbulence Model Development and Implementation For Low Pressure Turbines Using a Machine Learning Approach. PhD thesis, University of Melbourne, 2019.

41. Arnone, A.; Liou, M.S.; Povinelli, L.A. Navier-Stokes Solution of Transonic Cascade Flows Using Non-Periodic C-Type Grids. *J. Propuls. Power* **1992**, *8*, 410–417.